

## RESEARCH ARTICLE

10.1002/2014JD021965

## Key Points:

- Convective features in PRD during warm season
- Monthly variation of diurnal cycle, depth, and distribution of convection
- Mechanisms of coastal convection in PRD

## Correspondence to:

K. Zhao,  
zhaokun@nju.edu.cn

## Citation:

Chen, X., K. Zhao, and M. Xue (2014), Spatial and temporal characteristics of warm season convection over Pearl River Delta region, China, based on 3 years of operational radar data, *J. Geophys. Res. Atmos.*, 119, 12,447–12,465, doi:10.1002/2014JD021965.

Received 5 MAY 2014

Accepted 10 OCT 2014

Accepted article online 13 OCT 2014

Published online 18 NOV 2014

## Spatial and temporal characteristics of warm season convection over Pearl River Delta region, China, based on 3 years of operational radar data

Xingchao Chen<sup>1</sup>, Kun Zhao<sup>1</sup>, and Ming Xue<sup>1,2</sup>

<sup>1</sup>Key Laboratory for Mesoscale Severe Weather/MOE and School of Atmospheric Science, Nanjing University, Nanjing, China, <sup>2</sup>Center for Analysis and Prediction of Storms and School of Meteorology, University of Oklahoma, Norman, Oklahoma, USA

**Abstract** This study examines the temporal and spatial characteristics and distributions of convection over the Pearl River Delta region of Guangzhou, China, during the May–September warm season, using, for the first time for such a purpose, 3 years of operational Doppler radar data in the region. Results show that convective features occur most frequently along the southern coast and the windward slope of the eastern mountainous area of Pearl River Delta, with the highest frequency occurring in June and the lowest in September among the 5 months. The spatial frequency distribution pattern also roughly matches the accumulated precipitation pattern. The occurrence of convection in this region also exhibits strong diurnal cycles. During May and June, the diurnal distribution is bimodal, with the maximum frequency occurring in the early afternoon and a secondary peak occurring between midnight and early morning. The secondary peak is much weaker in July, August, and September. Convection near the coast is found to occur preferentially on days when a southerly low-level jet (LLJ) exists, especially during the Meiyu season. Warm, moist, and unstable air is transported from the ocean to land by LLJs on these days, and the lifting along the coast by convergence induced by differential surface friction between the land and ocean is believed to be the primary cause for the high frequency along the coast. In contrast, the high frequency over mountainous area is believed to be due to orographic lifting of generally southerly flows during the warm season.

### 1. Introduction

During the warm season from May through September, associated with the northward movement of the western Pacific subtropical high (WPSH hereafter), more warm and moist air is transported from the ocean onto the continent of China, increasing convective instability in the region. As a result, heavy rainfall events dominate the weather over south China during the warm season [Chen and Yu, 1988; Cho and Chen, 1995; Chen and Tseng, 2000; Xu et al., 2009; Zhang and Qi, 2010; Xu et al., 2012; Yu and Li, 2012]. Apart from frequent thermally induced convection, convection produced by weather systems including tropical cyclones (TCs) and Meiyu front (A Meiyu front is a quasi-stationary front between the northwest Pacific subtropical high and the midlatitude weather systems. It typically extends all the way from south Japan to southwest China and is characterized by wind shifts, strong moisture gradients, and relatively weak temperature gradients across the front [Chen and Chang, 1980]. Meiyu fronts are typically associated with persistent precipitation that can episodically last for about 1 month. Over the continental China, a Meiyu front is often referred to as the south China quasi-stationary front when it is located over southern China in the spring, and Meiyu season, most of the times refers to the precipitation season when the front is located in the Yangtze–Huaihe River Basin further north [Ding, 2010].) is also very common in the region [Chen et al., 2011]. Compared to the Yangtze–Huaihe River Basin, another region with concentrated warm season precipitation in China, precipitation occurs more frequently, and rainfall accumulations are larger in south China. In south China, mesoscale convective systems (MCSs) are dominant rainfall producers accounting for approximately 90% of the total rainfall during monsoon active periods [Luo et al., 2012]. Several regions of climatological rainfall maxima can be found in south China during warm season, and many of them are related to local topographic lifting and blocking effects [Xu et al., 2009; Xu et al., 2012; Xu, 2013].

Previous studies have found that the Pearl River Delta (PRD, shown by the dashed square in Figure 1) region, especially near the coast, is a climatological center of rainfall maximum in south China. Heavy precipitation

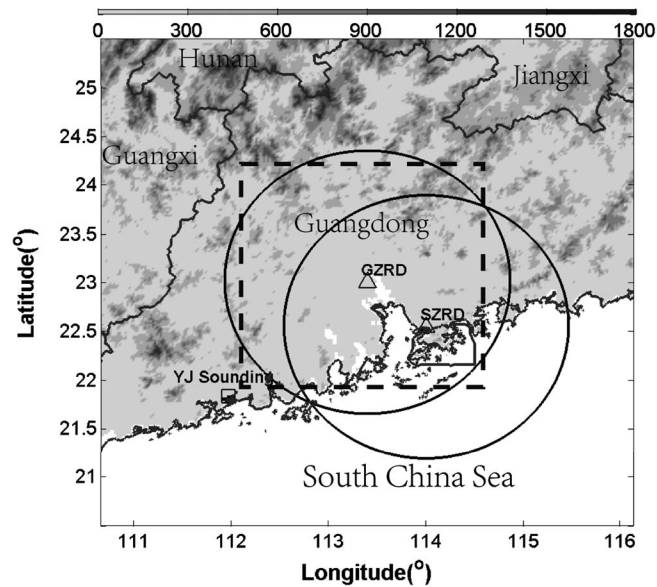


**Figure 1.** Locations of the Guangzhou (GZR) and Shenzhen (SZR) radars and Yangjiang (YJ) sounding station (black square). Pearl River Delta (PRD) is marked by dashed square. Orography is shown in gray scale. Coast lines and provincial borders are shown, together with the 150 km range circles of the two radars.

for a large percentage of total warm season rainfall in the region [Xu *et al.*, 2009; Liu and Fu, 2010; Chen *et al.*, 2011; Luo *et al.*, 2012; Xu, 2013].

Studies on the triggering and organizing mechanisms of warm season convection in PRD have mostly been based on individual cases [e.g., Zhu *et al.*, 2010; Sun, 2012]. Systematic studies based on a large number of cases in a statistical sense are lacking so far. Xu *et al.* [2009] hypothesized that orographic effects were the main causes of several climatological rainfall centers in south China. In contrast, convective rainfall in the relatively flat PRD region is to a less extent affected by orographic lifting or blocking (There is almost no mountain in the central part of PRD, and the highest mountain in our research area is below 1500 m.), but its mean rainfall amount is equal to or even higher than those aforementioned rainfall centers [Xu *et al.*, 2009]. The cause of the PRD rainfall center is not well known.

The rain gauge and satellite-based (e.g., TRMM) rainfall observations used in most of the previous studies have relatively low spatial and/or temporal resolutions. A TRMM satellite has only two overpasses per day at a particular location. The observations from the Chinese operational radar network in recent years provide a new opportunity to better resolve the spatial structures of precipitation, to better characterize the temporal variations of rainfall, and to allow us to better understand the triggering and development mechanisms of such rainfall.

Taking advantage of the availability of 3 years of data from the operational Doppler radar at Guangzhou, China (GZR in Figure 1), this study examines the detailed temporal and spatial distributions of convection over PRD during the warm season. Radar quantitative precipitation estimate products are used to calculate the convective rainfall contribution quantitatively. In addition, the radial velocity and its derived environmental wind profiles are used together with other data to help explain the physical mechanisms of coastal rainfall extremes in PRD. Such an approach has not been applied to this region before, to the best of our knowledge.

The rest of the paper is organized as follows: data and methodology used are introduced in section 2. Section 3 presents detailed spatial distributions for different types of convection in PRD. Monthly variations of diurnal cycle, vertical structures, and spatial distributions of convection in PRD together with the relationship between the monthly variations and changing atmospheric conditions are discussed in section 4. In section 5, relationships between low-level jets and the triggering of coastal convection are considered. Conclusions are given in section 6.

can bring loss of life and property and urban inundation in south China almost every year. Using hourly rain gauge records and Tropical Rainfall Measuring Mission (TRMM) 3B42 products from 1998 to 2006, Yuan *et al.* [2010] documented the diurnal characteristics of summer rainfall over subtropical East China. For the PRD region, they found that the mean daily precipitation was more than 10 mm in summertime. Using Precipitation Estimation from Remote Sensing Information using Artificial Neural Network TRMM 3B42 satellite products and rain gauge records, Zhou *et al.* [2008] found that PRD had very high mean rainfall amount (11 mm/d) and intensity ( $2.2 \text{ mm h}^{-1}$ ) and a daily occurrence frequency of 25% from June to August. Studies have also found that the occurrence frequency of deep convection is also high in PRD during warm season [Zhu *et al.*, 2010; Zheng and Chen, 2011]. Convective rainfall accounts

## 2. Data and Methods

### 2.1. Radar Data

The radar data used in this study are collected by two China's Weather Surveillance Doppler-1998 (CINRAD WSR-98D) radars at Guangzhou (GZRD) and Shenzhen (SZRD in Figure 1), operated by the China Meteorological Administration (CMA). Radar data collected by GZRD from the 2007 to 2009 warm seasons are used. Data from SZRD are used for the analysis of coastal convection only. These radars have a 10 cm wavelength (*S* band) with a 1° beam width and were operated in the VCP21 (volume coverage pattern 21) scanning mode, the same as the VCP21 mode of the WSR-88D radars of the United States. VCP21 consists of nine elevations between 0.5° and 19.5° [Crum *et al.*, 1993]. The maximum Doppler range is 230 km with a range resolution of about 1 km (250 m) in the radial direction for radar reflectivity (radial velocity) data. Like WSR-88D radars, the WSR-98D systems calibrate reflectivity for every volume scan using internally generated test signals in order to maintain a calibration precision of 1 dB.

The GZRD radar is located in the center of the PRD region (Figure 1), and its coverage region is characterized as a plain surrounded by moderate-height (400–800 m) mountains and the coastline, data from GZRD are used to investigate the characteristics of convection in PRD. The SZRD radar is located near the coast of this delta; the radial velocity and reflectivity data from SZRD are used to make range-height indicator displays and to explain the possible triggering mechanisms of coastal convection.

We started from level 2 radar data, which contain radar reflectivity, radial velocity, and spectrum width data in polar coordinates [Crum *et al.*, 1993]. Contaminated radar reflectivity due to ground, mountain, or sea clutters and velocity alias were removed using an automatic quality control procedure following Zhang *et al.* [2004] and Zhang and Wang [2006]. After the quality control, the reflectivity data were then bilinearly interpolated onto constant altitude plane position indicators in Cartesian coordinates with a 1 km grid spacing in both horizontal and vertical [Mohr and Vaughan, 1979]. The Cartesian-based radar volumes cover 150 km × 150 km horizontally and 15 km vertically every 6 min.

### 2.2. Classification of Convective and Stratiform Features and Radar Quantitative Precipitation Estimation

The Cartesian-gridded reflectivity data of GZRD at the 3 km altitude are used in an algorithm based on Steiner *et al.* [1995] to separate the convective and stratiform parts of the radar echoes. Only the convective components are considered in this study. Since no disdrometer data are available to tune the classification criteria, we assume that the parameters used in Steiner *et al.*'s [1995] paper hold in our study region. The first step of classification is to label all grid points (and associated cell volumes) with a reflectivity of at least 40 dBZ convective. Then, grid points with reflectivity exceeding the average value within an 11 km radius of a convective grid point labeled as such in the first step by a specified amount (this criterion is given in Figure 7 of Steiner *et al.* [1995]) are also identified as convective. Finally, for each convective grid point, all surrounding grid points within an intensity-dependent radius are also identified as convective. Based on the concept of convective precipitation features [Romatschke *et al.*, 2010], a convective feature is defined as being consisted of contiguous convective grid points at the 3 km altitude, extending vertically in each column to include grid points from the echo base to the echo top. The convective features with horizontal areas smaller than 20 km<sup>2</sup> are removed from the data set. After the convective features are identified, their vertical structures, spatial distributions, and temporal variations are studied.

Based on the precipitation-type classification, different *Z-R* relations are used to compute the rain rate at each grid point for each volume scan, similar to Xu *et al.* [2008]. For convective echo, relationship  $Z = 300 R^{1.4}$  [Fulton *et al.*, 1998; Ulbrich and Lee, 1999] is used, and for stratiform echo,  $Z = 200 R^{1.6}$  [Marshall and Palmer, 1948] is applied (*Z-R* relationships are used by CMA now). The convective and stratiform rainfall totals estimated from the reflectivity data are then accumulated separately at each grid point for the 3 years, and the total rainfall is their sum.

### 2.3. Velocity-Azimuth Display Winds

To investigate the characteristics of low-level jets (LLJs) over the PRD region, we used the velocity-azimuth display (VAD) wind data of GZRD. VAD is a technique for deriving vertical profiles of horizontal wind as well as other properties of the wind fields from single-Doppler-radar radial velocity measurements [Browning and

Wexler, 1968]. The radial velocity measurements are obtained by scanning the radar beam about a vertical axis at a fixed elevation angle. Harmonic analysis of VAD permits divergence to be obtained from the magnitude of the “zeroth” harmonic, wind speed and direction are obtained from the amplitude and phase of the first harmonic, and resultant deformation and the axis of dilatation are obtained from the amplitude and phase of the second harmonic. Many previous studies [e.g., Nelson *et al.*, 1995; Holleman, 2005] have analyzed the accuracy of VAD winds by comparing them with collocated radiosonde wind data. Their results show that VAD winds are generally in a good agreement with sounding observations, with root-mean-square errors below  $2 \text{ m s}^{-1}$ . Given the high-volume scan frequency of radar data, VAD winds at 6 min intervals are obtained and used in this study.

#### 2.4. Other Data

We also used two other observational data sets in this study. Data from surface automatic weather stations (954 of them in PRD) are used to investigate the possible physical mechanisms for the triggering of coastal convection. In addition, Japan Meteorological Agency (JMA) East Asia reanalysis data sets are used to characterize the statistical conditions over the area of interest in different months. These reanalysis data have a horizontal resolution of  $0.25^\circ \times 0.2^\circ$  and are available at 00:00, 06:00, 12:00, and 18:00 UTC each day [Saito *et al.*, 2006].

### 3. Spatial Distributions of Convective Features

In this section, convective rainfall fraction is first analyzed. The spatial distributions of convective features for the entire warm seasons are examined. The convective features are also divided into six categories according to their area coverage and depth, and the spatial distributions of the categories are compared.

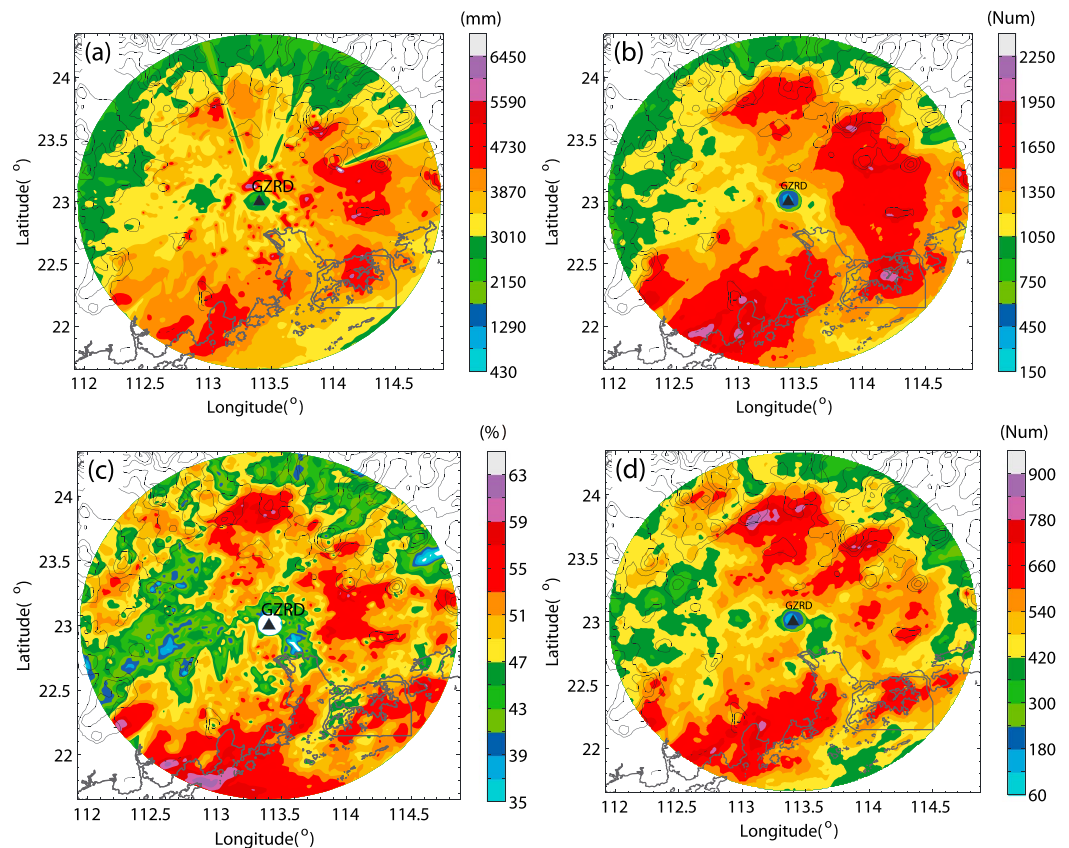
#### 3.1. Spatial Distributions of All Convective Features

Figure 2a shows the 3 year accumulated rainfall in PRD throughout the warm seasons. There are two high-precipitation regions: located along the southern coastal area and on the windward slope of the north and northeastern mountainous area. The spatial distribution of the occurrence frequency of convective features is shown in Figure 2b. The occurrence frequency at each grid point is counted as the total number of times that the grid point is covered by convective features within the 3 year warm seasons. In general, the spatial pattern of occurrence frequency corresponds well to the accumulated rainfall. The maxima of occurrence frequency are, as with rainfall, also generally found on the windward (prevailing winds or monsoon flows of the season are southwesterlies) slope of the northeastern mountainous region and along the southern coastal area. The percentage of convective rainfall contribution to total rainfall reaches nearly 60% in the coastal region, larger than the maximum of about 55% found in the mountainous area (Figure 2c).

It is well known that during the warm season (especially in the summer), the warm and moist southerly flows at the low levels prevail in PRD, and the corresponding level of free convection is low [Chen, 1983; Du *et al.*, 2014]. As a result, Luo *et al.* [2012] proposes that the orographic lifting alone is often enough for initiating convection on the windward slope, even though the orography in PRD is rather low with an average height below 500 m. For PRD, the enhanced rainfall along the coastline has also been noted by various previous studies [Xu *et al.*, 2009; Zhu *et al.*, 2010; Chen *et al.*, 2011; Zheng and Chen, 2011], but the exact cause is not clear. For other regions, the enhanced coastal rainfall had been shown to be caused by locally enhanced convergence resulting from differential surface friction or heating between land and ocean, sometimes associated with synoptic systems such as front and TC [e.g., Chen and Yu, 1988; Jou and Deng, 1998; Xu *et al.*, 2012]. Trying to understand the cause of enhanced coastal rainfall in the PRD region is part of the goals of this study; this will be discussed in section 5.3.

#### 3.2. Spatial Distributions of Convective Features of Different Sizes and Depths

Convective features of different sizes and vertical depths often occur in quite different synoptic conditions and may occur due to different reasons. It is therefore helpful to divide the convective features into different categories or groups and examine their statistical characteristics separately to gain more insight. We divide all convective features within our study period into six categories based on their area coverage and echo top height: Convective features with area coverage of more than  $400 \text{ km}^2$ , less than  $100 \text{ km}^2$ , and in-between are classified as large, small, and medium features, respectively, following the rules of classification used by Xu and Zipser [2012]. Because 15 dBZ is the minimum detectable signal of the radar, in order to get no



**Figure 2.** Spatial distributions of (a) 3 year accumulated rainfall during the warm season, (b) the occurrence frequency of convective features, (c) percentage of convective rainfall events, and (d) number of convective features under weak synoptic forcing. Orography is superimposed in the figure in black contours with 150 m intervals.

radial biasing of storm top height, we use 15 dBZ to define the radar echo top. Convective features whose echo top is higher than 12 km is called deep convection, following *Zhang et al.* [2006], and those with echo top lower than 6 km are called shallow convection. In the south China MeiYu season, the melting level height is typically around 6 km [*Xu et al.*, 2009; *Xu and Zipser*, 2012], so shallow convection in the region is dominated by warm rain processes with few lightning flashes. Convective features having echo tops between 6 and 12 km are defined as medium depth features.

For small convective features, there appears to be no clearly preferred location or organization of convection in the region, apart from the generally higher frequencies surrounding the radar (Figure 3a). The decrease in the frequency away from the radar appears to be due to the lowest radar scan overshooting the top of small-sized echoes at longer distances. This uniform distribution reflects the random occurrence nature of small convective features in warm season (Figure 3a). For medium sized convection, two frequency centers of convective features on the windward slope of eastern mountains and along the coastline are evident (Figure 3b), and they are clearer for large convection (Figure 3c).

A similar trend can also be found with the increase in the depth of convection. Shallow convective features are less organized but occur more frequently along the coastline and on the southern slope of mountains, and over PRD close to the radar (Figure 3d). The donut-shaped ring surrounding the radar site in Figure 3d is of high frequency because the highest radar elevation is below 6 km within this ring. With the increase in the depth of features, the spatial distribution pattern becomes more and more like that of large features (Figures 3e and 3f), which reflect the more systematic behaviors of larger, deeper convective features. The prominent hole at the center of Figure 3f is due to the “cone of silence” of radar measurement, where the highest radar elevation is limited to the lower levels near the radar. The frequency distributions suggest important roles played by orographic and coastline forcing.

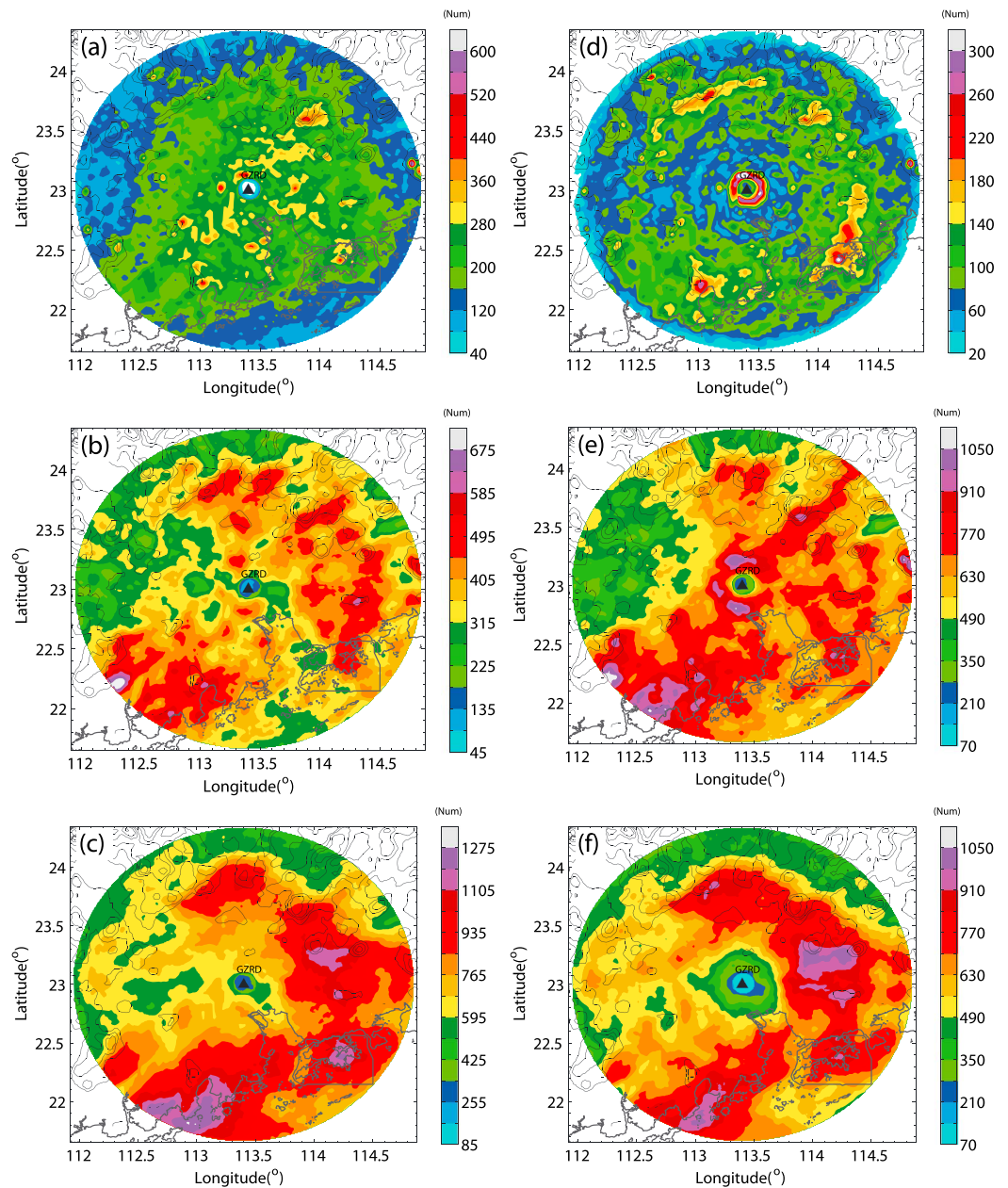


**Figure 3.** Occurrence frequency distributions of (a) small, (b) medium, (c) large, (d) shallow, (e) medium depth, and (f) deep convective features. Orography contours are superimposed with 150 m intervals.

#### 4. Monthly Variations

PRD has a humid subtropical monsoon climate. During the warm season, with the northward movement of the WPSH, the climatic features and synoptic forcing differ greatly from other seasons [Chen and Chang, 1980; Chen et al., 2011; Zhang et al., 2011; Zheng and Chen, 2011; Luo et al., 2012]. Mid-May through mid-June is the typical south China Meiyu season. Our study region is occupied by warm and moist air from the ocean, and a quasi-stationary Meiyu front can usually be found during this period [Xu et al., 2009]. In July and August, PRD is located south of the westward extending ridge of the WPSH, and the solar heating effect is the strongest and the TC influence is common during the period. In September, temperature and precipitation in PRD begin to decrease, and cold air from the north begins to influence the region. Due to these climatological characteristics during the 5 months, characteristics of convective features also change from month to month.

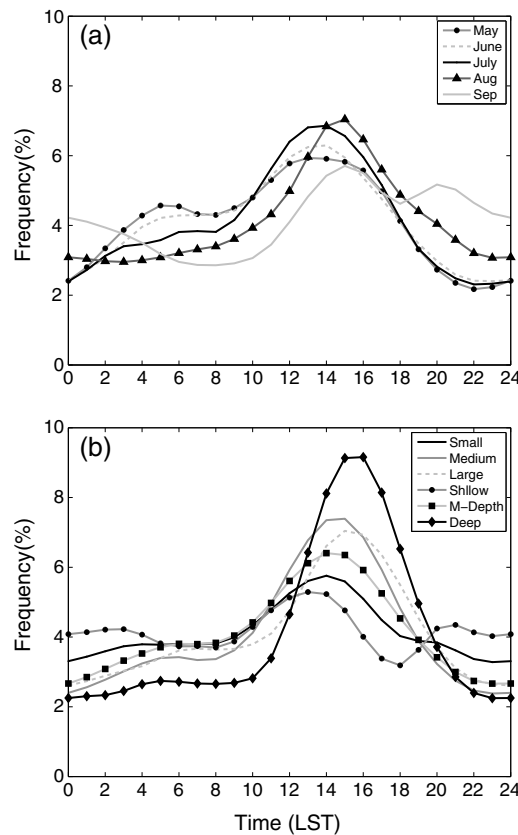


**Figure 4.** Diurnal cycles of convection occurrence frequency for (a) each of the five warm season months and (b) for convective features of different sizes and depths in years 2007 through 2009. The horizontal axis is time in LST (local standard time).

Figure 4a shows the diurnal cycles of convective feature occurrence frequency in PRD for each of the five warm season months averaged for 2007 through 2009. It is seen that in all months, convective features occur most frequently in early afternoon around 14:00–15:00 local standard time (LST hereafter). This early afternoon peak is obviously closely related to solar heating [Romatschke and Houze, 2011; Luo et al., 2012]. August and July show the most prominent, single peak throughout the 24 h; May and June (early summer or during the south China Meiyu season) have a secondary peak in early morning, while September (late summer) has a secondary peak in early evening. Xu and Zipser [2011] also noted a secondary peak in early morning during pre-Meiyu to Meiyu season (May–June) in the region based on satellite data, and they hypothesized it to be related to the influence of synoptic-scale systems. Propagation of convective systems initialized elsewhere can also create local secondary precipitation peaks [e.g., Yu and Jou, 2005; Romatschke et al., 2010]. The exact cause of the secondary peak found here will require further study.

In July and August, the region is often controlled by the WPSH, and the early afternoon convective rainfall is closely related to local instability due to solar heating. The triggering mechanisms of evening convection in September is less clear; it may be related to propagating convective systems interacting with local features, although the exact mechanism will require more in-depth investigations that can be a topic for future studies.

The occurrence frequency diurnal cycle of convective features with different sizes and vertical depths are also compared in Figure 4b. All convective features occur most frequently in early afternoon due to solar heating effects. In general, deeper and/or larger convective features have more prominent early afternoon peaks than shallower and/or smaller features. At the same time, the peaks of deeper and/or larger features occur 2–3 h later than the shallower and/or smaller ones. This time lag appears to be because more intense convection tends to take more time to accumulate more instability or convective energy from surface heating, which when eventually released (possibly by breaking a cap or capping inversion) produces stronger convection.

#### 4.2. Monthly Variations of Vertical Structure

Figure 5 shows the vertical profiles of maximum radar reflectivity (VPRR) of convective features in different months. We used the same definition of VPRR as in Donaldson [1961], where it was defined as the maximum

To better understand the characteristics of convective features over PRD, it is also important to analyze these features month by month. In this section, the diurnal cycle, vertical structure, spatial distribution, and related synoptic patterns for each of the 5 months are discussed.

#### 4.1. Monthly Variations of Diurnal Cycle

Diurnal variation is one of the most important characteristics of convection. Many researchers have investigated the rainfall diurnal cycles in south China based on long-term rain gauge data [Li et al., 2008; Zhou et al., 2008; Yuan et al., 2010] and satellite data [Xu and Zipser, 2011; Luo et al., 2012]; they have found that the behaviors of diurnal cycles in south China change as the season progresses. As pointed out earlier, the high temporal resolution of radar data enables us to examine diurnal cycles with much greater accuracy than, e.g., the much less frequent satellite data on which most past precipitation climatology studies used.

Figure 4a shows the diurnal cycles of convective feature occurrence frequency in PRD for each of the five warm season months averaged for 2007 through 2009. It is seen that in all months, convective features occur most frequently in early afternoon around 14:00–15:00 local standard time (LST hereafter). This early afternoon peak is obviously closely related to solar heating [Romatschke and Houze, 2011; Luo et al., 2012]. August and July show the most prominent, single peak throughout the 24 h; May and June (early summer or during the south China Meiyu

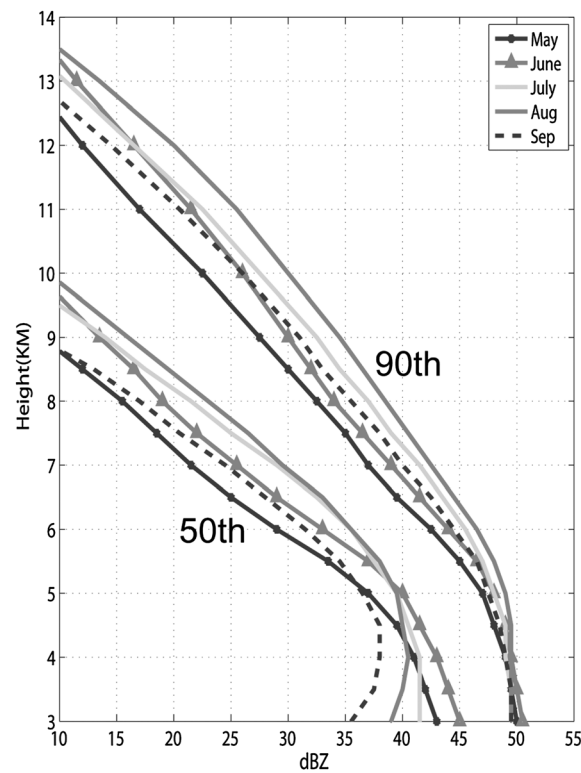


**Figure 5.** Vertical profiles of 50th and 90th percentile maximum radar reflectivity (VPPR) of convective features in different months. Only profiles above 3 km agl are plotted because of the local radar data coverage at the lower levels away from the radar.

speaking, the median maximum reflectivity in September was the weakest, corresponding to less intense solar heating or weaker synoptic-scale forcing.

In terms of the 90th percentile reflectivity, convection in different months has almost the same vertical profiles below 5 km; the 90th percentile reflectivity reaches 50 dBZ at the 3 km height level, and their values are similar below 4 km in all months. As the season progresses from May through August, there is a consistent tendency for convection to become deeper, with the 90th percentile profiles reaching levels that are about 1.5 km higher in August than in May. By September, the depth of convection decreases to levels more comparable to those of June and July, corresponding to generally weaker convection.

*Xu et al.* [2009] compared the vertical structures and properties of MCSs and sub-MCSs (smaller sized MCSs) a priori to, during and after Meiyu season by compositing 10 year TRMM measurements. They found that very intense convective cells within MCSs during Meiyu are comparable to those after Meiyu, while convective cells in sub-MCSs are much weaker than those during post-Meiyu. Similar characteristics can be seen in our study. The PRD region is affected by southwesterly winds at the low levels due to the onset of south China summer monsoon in May and June, especially in June. Meiyu fronts are often present during this period, so convective systems during early summer can be considered convection in Meiyu season. In midsummer (July and August), with the northward shifting of WPSH and the movement of Meiyu front to the Yangtze–Huaihe River Basins, PRD becomes controlled by WPSH and the characteristics of convection over PRD become closer to those of post-Meiyu convection. Evidences can be found from the above discussions on diurnal cycles and vertical structures of reflectivity: convection in early summer is shallower than convection in middle summer, consistent with the findings of *Xu et al.* [2009], and the early summer convection has a secondary diurnal peak in early morning.

### 4.3. Monthly Variations of Spatial Distributions

Besides the monthly variations in diurnal cycles and in the vertical structures of convection over PRD, monthly variations in spatial distribution are also dramatic (Figure 6). At the first sight, we can see that June

reflectivity within convective features as a function of height. VPPR is often used as an indicator of storm intensity or lightning probability [Donaldson, 1961; Szoke and Zipser, 1986; Zipser and Lutz, 1994; Xu et al., 2009]. Two sets of vertical profiles represent 50th and 90th percentiles of maximum radar reflectivity of convective features at each height over PRD in different months. The 90th percentile VPPR represents the top 10% maximum radar reflectivity at each height, while the 50th percentile VPPR represents the median maximum radar reflectivity at each height. The absence of a bright band in Figure 5 indicates that the Steiner algorithm effectively isolates the stratiform regions.

In terms of the 50th percentile (median) maximum reflectivity, convection in June and May is stronger at the middle-to-low levels than in other months. The median intensity reflectivity in June can reach 45 dBZ at the 3 km height, and the intensity decreases quickly with height. On the other hand, convection in July and August has the strongest reflectivity among the 5 months above 5.5 km. Although the median intensity at the 3 km height is weaker at about 40 dBZ in July and August, it remains more or less constant below 5.5 km. Generally

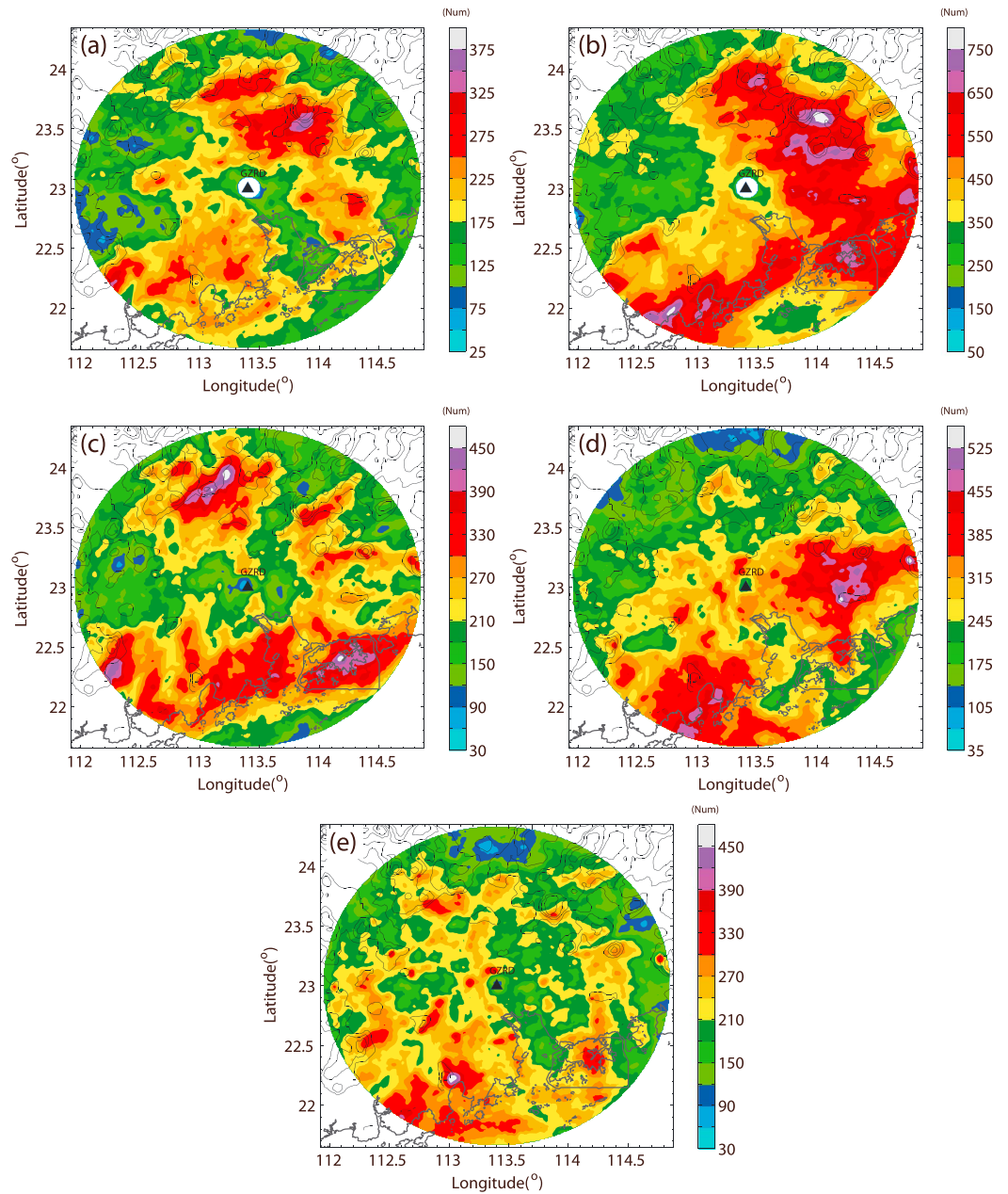


**Figure 6.** Spatial distribution of convection occurrence frequencies in different months: (a) May, (b) June, (c) July, (d) August, and (e) September. Orography is superimposed on the figure in black contours with 150 m intervals.

has two frequency maxima of convective region, on the windward slope of the northeastern mountains and along the coastline, respectively. In May, the maximum along the coastline is less obvious, while August and September have no prominent inland frequency maximum. We can also see that the exact locations of frequency maxima on the mountain slope are also different in different months, which should be related to the monthly changes in the prevailing winds at the low levels; the low-level prevailing winds change from southwesterly to more southerly as the season progresses, which can be seen in the reanalysis data (Figure 7, middle column). Figure 6 also shows that the total occurrence frequency is the highest in June and the lowest in September among the 5 months (note the scale differences in the color bars). The highest convection frequency in June can be attributed to the Meiyu front that usually lasts from late May to the end of June in the region.

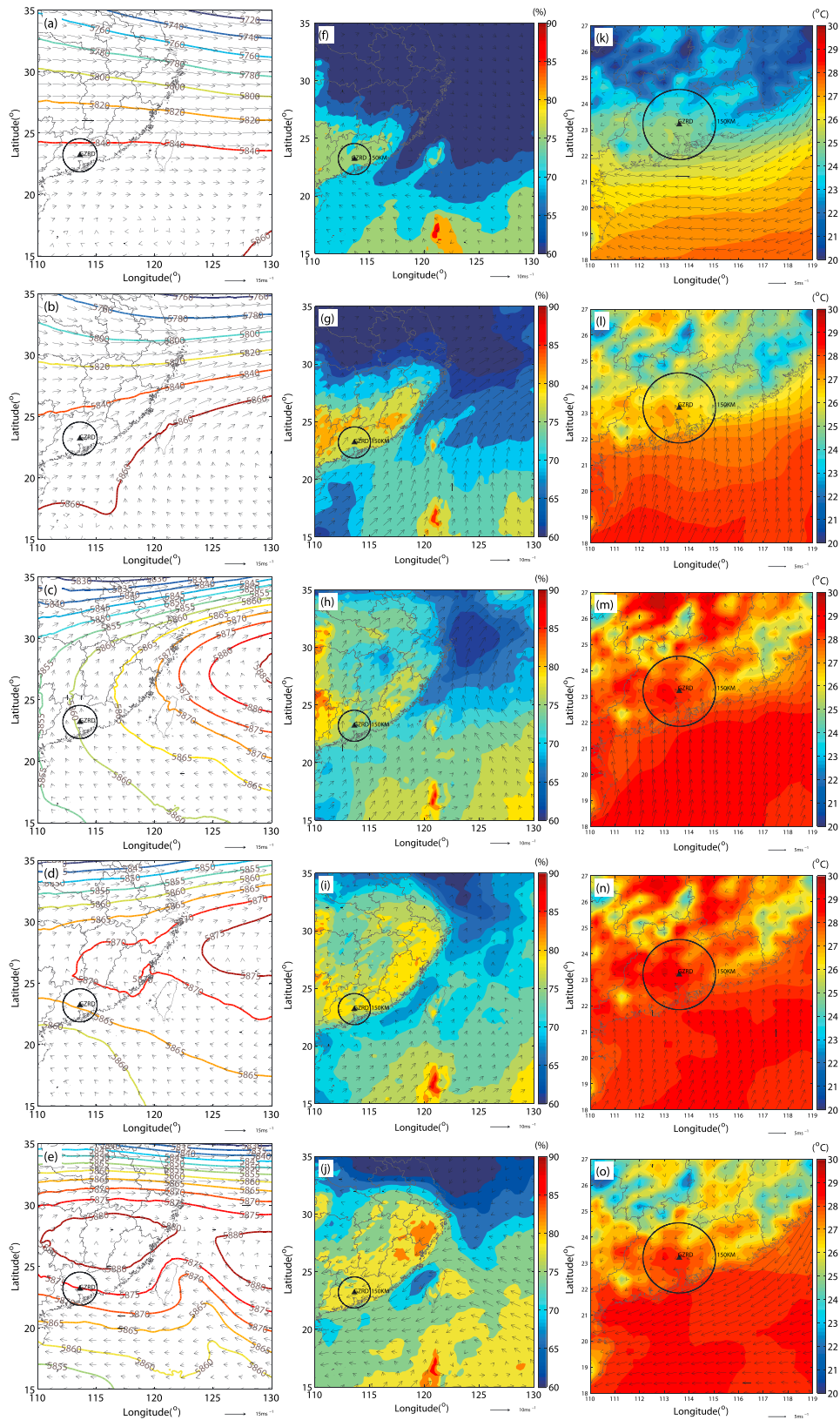


**Figure 7.** (left column) The mean pressure (contours) and wind (arrows) fields at 500 hPa, (middle column) the relative humidity (color filled contours) and wind (arrows) fields at 850 hPa, and (right column) the surface temperature (color filled contours) and surface wind (arrows) fields for the months of (top to bottom row) May through September.

#### 4.4. Monthly Variations of Weather Pattern

The monthly variations in diurnal cycles, the vertical structures, and spatial distributions of convection have close relationships with the large-scale flow and atmospheric conditions. Based on the JMA reanalysis data set, monthly mean (averaged over 00, 06, 12, 18 UTC data of each day) synoptic maps are shown in Figure 7 for 500 and 850 hPa levels and at the surface.

Figure 7 (left column) shows that the prevailing winds in the middle troposphere change from month to month with the northward migration of WPSH. The PRD region is covered by the prevailing westerly winds in May, and WPSH is mostly south of 15°N. June is the Meiyu season of south China, and during the month, WPSH is located off the southeast China coast with the midlevel prevailing winds over south China coming from the southwest. In July and August, the Meiyu front has moved to the Yangtze–Huaihe River Basins, and our study region is located west-southwest of the WPSH center and the region is dominated by south-southeasterly winds at the midlevels. By September, with the further northward and westward migration of WPSH, PRD is mostly on the south side of WPSH, and the prevailing midlevel winds are mostly easterly.

As with the large-scale flow changes at 500 hPa, wind direction also changes dramatically from month to month at 850 hPa (middle column of Figure 7). In May, winds mainly blow from the east, and the mean relative humidity in PRD is around 75% (which is the lowest among the months). In June, with the establishment of south China summer monsoon, the prevailing wind direction changes to the southwesterly, and the mean relative humidity increase markedly to around 80% at 850 hPa. The prevailing winds change to south-southeasterly by midsummer and become northeasterly in September. Generally speaking, the relative humidity at the 850 hPa level is high during the entire warm season.

Monthly variations at the surface are also prominent (Figure 7, right column). The mean surface temperature continuously increases from May through August. The maximum average temperature reaches 30°C in August, and strong solar heating is an important forcing for deep convection in the month. Like the middle and low levels, the surface prevailing winds also dramatically change from month to month. Northeasterly winds dominate at the coastline of PRD in May. Surface winds are mostly perpendicular to the coastline in June, July, and August, coming onshore from the south. In September, surface winds are mostly parallel to the coastline, coming from the northeast. We can see obvious velocity convergence along the coastline, especially in June through August when the onshore wind speeds decrease significantly when the winds reach the land; the increased roughness over land is obviously the cause for the deceleration. In June, we see the strongest temperature gradient near the coastline as the temperature off the coast has significantly increased while the land remains relatively cold. The temperature contrast is about 2–3°. In May, the land is even colder, and the temperature contrast along the coast has a similar magnitude. Such temperature contrasts can produce sinusoidal (mean land breeze) circulations that can trigger and support convection; the fact that May and June have stronger temperature contrasts across the coastline supports the earlier suggestion that land-sea breeze circulations may be responsible for the early morning secondary peaks of convection seen in Figure 4 in these 2 months, although the exact processes by which the second peaks are produced require more detailed investigations.

### 5. Possible Mechanisms of Coastal Convection

The statistics in the previous sections indicate that larger, deep convection mostly occur along the coastline and on the windward slope of the mountains in the PRD region, when the region is dominated by southerly south China monsoon flows at the low levels. The southerly flows can be further enhanced by the presence of low-level jets (LLJs). In this section, we look at how LLJs affect convection in the PRD region and suggest possible mechanisms for localized precipitation enhancements.

#### 5.1. Characteristics of Low-Level Jets

LLJs have been found to have a close relationship with heavy rainfall in south China during warm season [Chen and Yu, 1988; Jou and Deng, 1992; Chen *et al.*, 1994; Jou and Deng, 1998; Chen *et al.*, 2005]. They can transport abundant warm, moist, and unstable air from ocean to land. On days under the influence of LLJs, atmospheric stability usually decreases dramatically, and quasi-stationary (often Meiyu) fronts are often found on the northern fringe of LLJs.

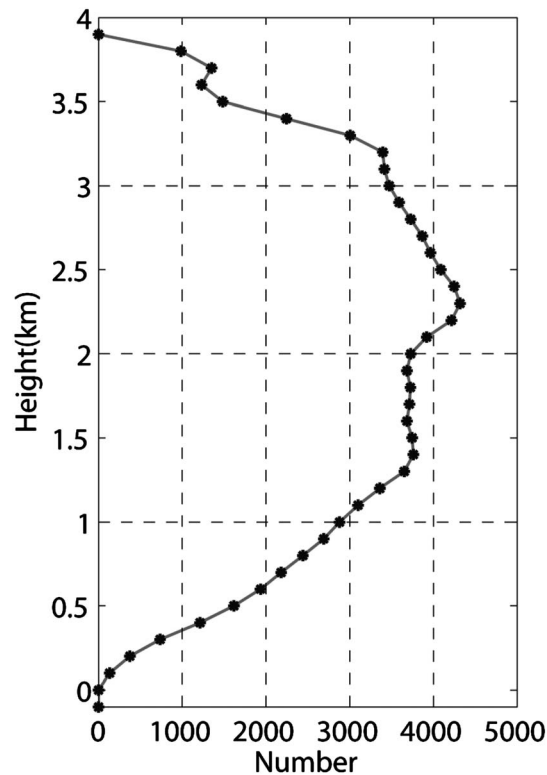


**Figure 8.** Vertical profiles of the occurrence frequency of low-level jet based on the VAD wind profiles from Guangzhou radar for May–September months of 2007–2009.

Du *et al.* [2012] used data from the Qingpu wind profiler radar to investigate the characteristics of LLJs over the coastal areas of East China and their linkages with rainfall during warm season. Two peaks of the LLJ incidences were found at the 500–800 m and 2100–2200 m altitudes (above ground level (agl)), which they referred to as the boundary layer LLJs and synoptic-system-related LLJs. They also found that both jets are present more often on rainy days. Similar results were also found by Chen *et al.* [2005] by using 12-hourly sounding data. Besides height, they also classified LLJs based on their appearance and movement. They pointed out that before and near the onset of more severe heavy rain events ( $>100$  mm/24 h) in northern Taiwan, there was a 94% chance that a LLJ would be present over an adjacent region at 850 hPa and a 88% chance at 700 hPa.

VAD wind data from GZRD provide wind profiles every 6 min and are excellent for studying the characteristics of LLJs over our research region. The criteria we used to identify LLJ incidences are similar to those of Chen *et al.* [2005]; they are the following: (1) maximum wind speed is  $\geq 12.5$   $\text{ms}^{-1}$ , (2) direction of the maximum wind is between  $180$  and  $270^\circ$  (southerly to westerly), and (3) vertical shear below and above the maximum wind is  $\geq 1 \times 10^{-3}$   $\text{s}^{-1}$ .

Different from the vertical profiles of LLJ incidences in Taiwan and Qingpu, we find that LLJs in PRD have only one peak at the 2300 m altitude (Figure 8). Following previous studies, we believe that this peak is the synoptic-system-related LLJs which influence south China every summer [Li and Chen, 1998]. Different from Taiwan where a barrier-layer jet is often found at an  $\sim 500$  m altitude, PRD has no LLJ peak below 1000 m. It may be related to the flat landscape around GZRD. Orographic blocking on the prevailing airflow at a low Froude number (Fr) flow regime can often produce barrier jet in the planetary boundary layer below 1 km, and this phenomenon can be found around the world with high topographies [Smith and Grubišić, 1993; Georgelin *et al.*, 1996; Douglas *et al.*, 1998; Igau and Nielsen-Gammon, 1998; Li and Chen, 1998; Skamarock *et al.*, 1999; Chelton *et al.*, 2000]. There is, however, no mountain higher than 500 m within a radius of 50 km of GZRD. There is no boundary layer jet in the Guangzhou VAD data.

## 5.2. Rainfall Spatial Distributions on LLJ and No-LLJ Days

To better separate diurnal and topographic effects from those of synoptic systems, we exclude the days when fronts, TCs, shear lines, and southwest vortices [Kuo *et al.*, 1988] exist within our analysis domain. Daily surface and upper level (850, 700, 500, and 200 hPa) weather maps from CMA are used to identify these features. With this exclusion, the occurrence frequencies of convective features are reduced to about half of total occurrence frequencies (Figure 2d), and the spatial distribution of convection is, however, still similar to the distribution without the exclusion (Figure 2b). The orographic forcing and coastal effects are therefore believed to dominate the distribution patterns of warm season convection over PRD.

Based on the presence or absence of LLJ, we divide all days that were not strongly influenced by synoptic systems in the warm seasons into LLJ days (21 days total) and no-LLJ days (251 days total). We then check the mean spatial distributions of convection occurrence frequency on the LLJ days and no-LLJ days.

Somewhat surprisingly, we find a prominent frequency maximum along the coastline but no frequency maximum inland on the LLJ days. In contrast, on the no-LLJ days, a region of convective frequency maximum

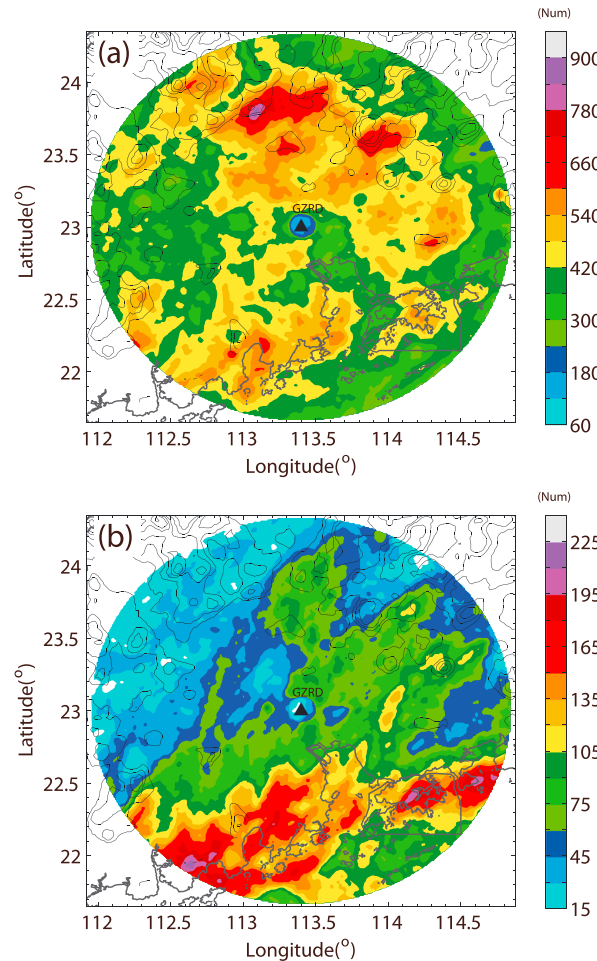


**Figure 9.** Spatial distributions of convection occurrence frequency on (a) no-LLJ days and (b) LLJ days. Orography is superimposed in black contours with 150 m intervals.

is found at the foot of the windward slope of the north/northeastern mountain area, while no obvious maximum is found along the coast (Figure 9). These results indicate that there is a close relationship between the LLJs and the occurrence of coastal convection over PRD.

**5.3. Possible Mechanisms**

We compare the mean weather patterns on LLJ and no-LLJ days based on the mean weather maps from the JMA reanalysis for the two types of days (Figure 10). WPSH is closer to PRD on LLJ days than on no-LLJ days, and the mean winds at 500 hPa are southerly on LLJ days and southwesterly on no-LLJ days (not shown). The air at the 850 hPa level is moister on LLJ days than on no-LLJ days on average (Figures 10a and 10d). The low-level prevailing wind directions are also different; the winds are southerly on LLJ days, which bring moister and warmer air to PRD from the ocean, while on no-LLJ days, the mean winds are weaker and are from the southeast.

At the surface, temperature contrast along the coast is larger, and the onshore winds are stronger on LLJ days (Figures 10b and 10e). It is obvious that the atmospheric conditions on LLJ days are more favorable for the triggering and maintenance of convection along the coast. Stronger and deeper updrafts at the coast (shown in color-filled contours in Figures 10c and 10f) can be found in the cross section along 114°E on LLJ days than on

no-LLJ days. On LLJ days, two downward branches of circulation or downdrafts are found on the north and south sides of the main updraft, respectively, with the northern, inland branch being much stronger and having a similar magnitude as the updraft. This inland downdraft, together with the updraft, forms a secondary vertical circulation (Figure 10f) that should promote convection at the coastline; the vertical circulation is much weaker on no-LLJ days (Figure 10c).

We also used automatic weather station (AWS) data to investigate the difference in boundary layer conditions between LLJ and no-LLJs days. The spatial distribution of AWS is shown in Figure 11a. We divide all automatic stations near the coastline into seaside and landside subregions, as indicated by the adjacent black rectangles in Figure 11a. The diurnal cycles of the mean offshore wind speed, temperature at the surface in the two subregions, and the mean precipitation in both subregions are examined.

Due to the prevailing southerly winds at the surface (Figures 10b and 10c), the average surface winds in PRD are onshore during the warm season. The diurnal changes of surface temperature and onshore winds during no-LLJ days are much more prominent than the corresponding changes on LLJ days. The early afternoon surface temperature peak is lower on LLJ days due to possibly the cooling effect of stronger coastal precipitation on those days (Figure 9) and possibly also due to the stronger advection of oceanic air inland. We can also see that the velocity convergence along the coastline (the solid black line – the dashed black line) in LLJ days is much stronger than the convergence in no-LLJ days. This stronger velocity convergence on the LLJ days and the resulting stronger coastal upward motion appear to be responsible for the convection occurrence frequency maximum along the coastline. On the other hand, on no-LLJ days, the coastal convergence is weaker,

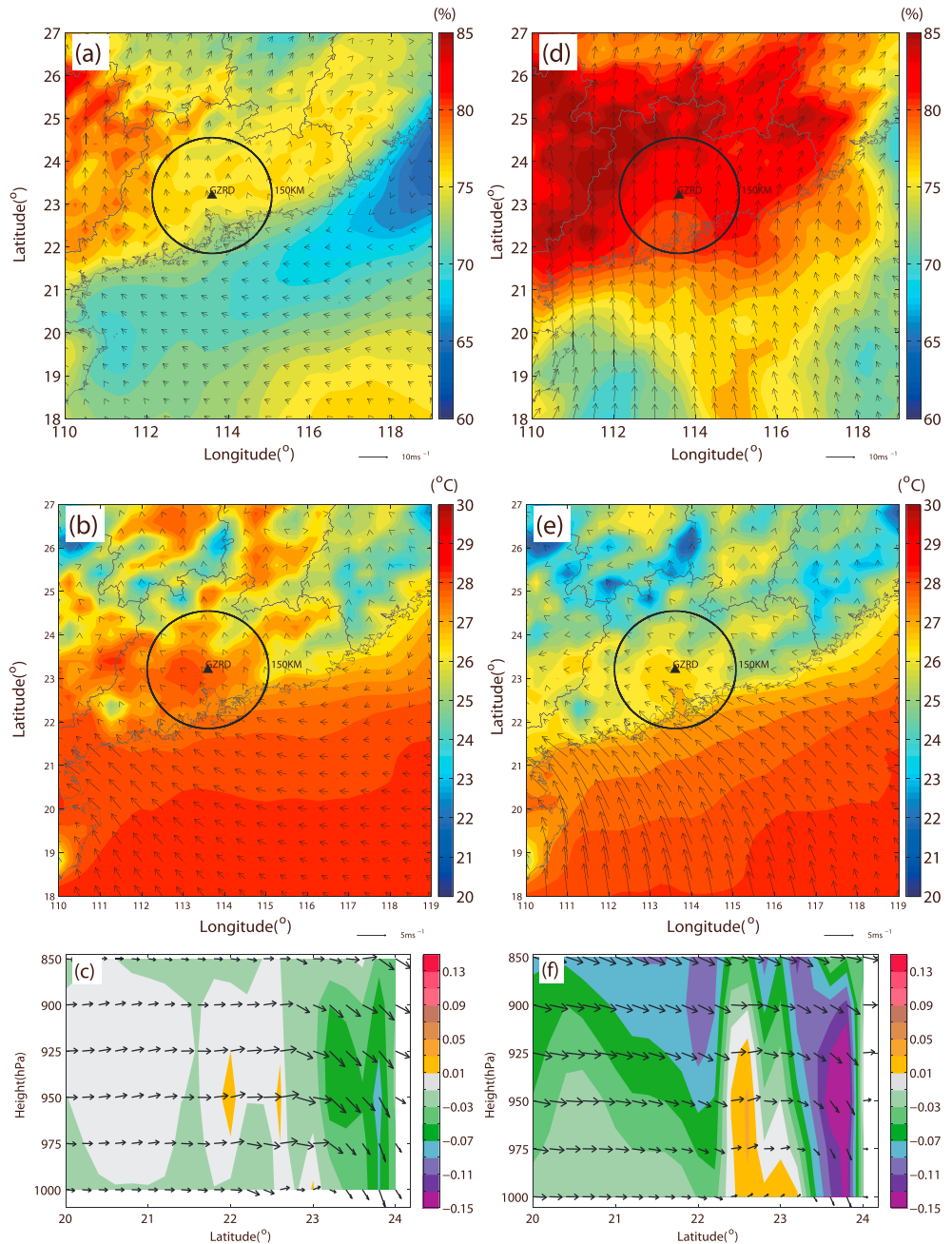


**Figure 10.** Relative humidity and wind fields at 850 hPa in (a) no-LLJ days and (b and e) LLJ days. The surface temperature and surface winds in (c and f) no-LLJ days and (d) LLJ days. Figures 10c and 10f are vertical cross-sections along the black lines in Figures 10b and 10e, respectively, and the color filled contours are for vertical velocity.

allowing the onshore flow to cross the coastal region without producing convection (hence preserving convective instability) and reach the mountain slope to the north where orographic lifting can trigger convection.

The precipitation in the coastal region (inside the black box in Figure 11a) also has different diurnal cycle patterns on no-LLJ and LLJ days. On no-LLJ days, coastal precipitation has no prominent afternoon peak. Several small rainfall peaks are found between 3 and 18 LST. Earlier morning precipitation is common on no-LLJ days. This character is very similar to that found in previous studies that offshore convection is often triggered by the collision between land-breeze and prevailing onshore winds during nighttime hours, and the convection propagates toward the coast slowly and dissipates before noon [Yu and Jou, 2005].

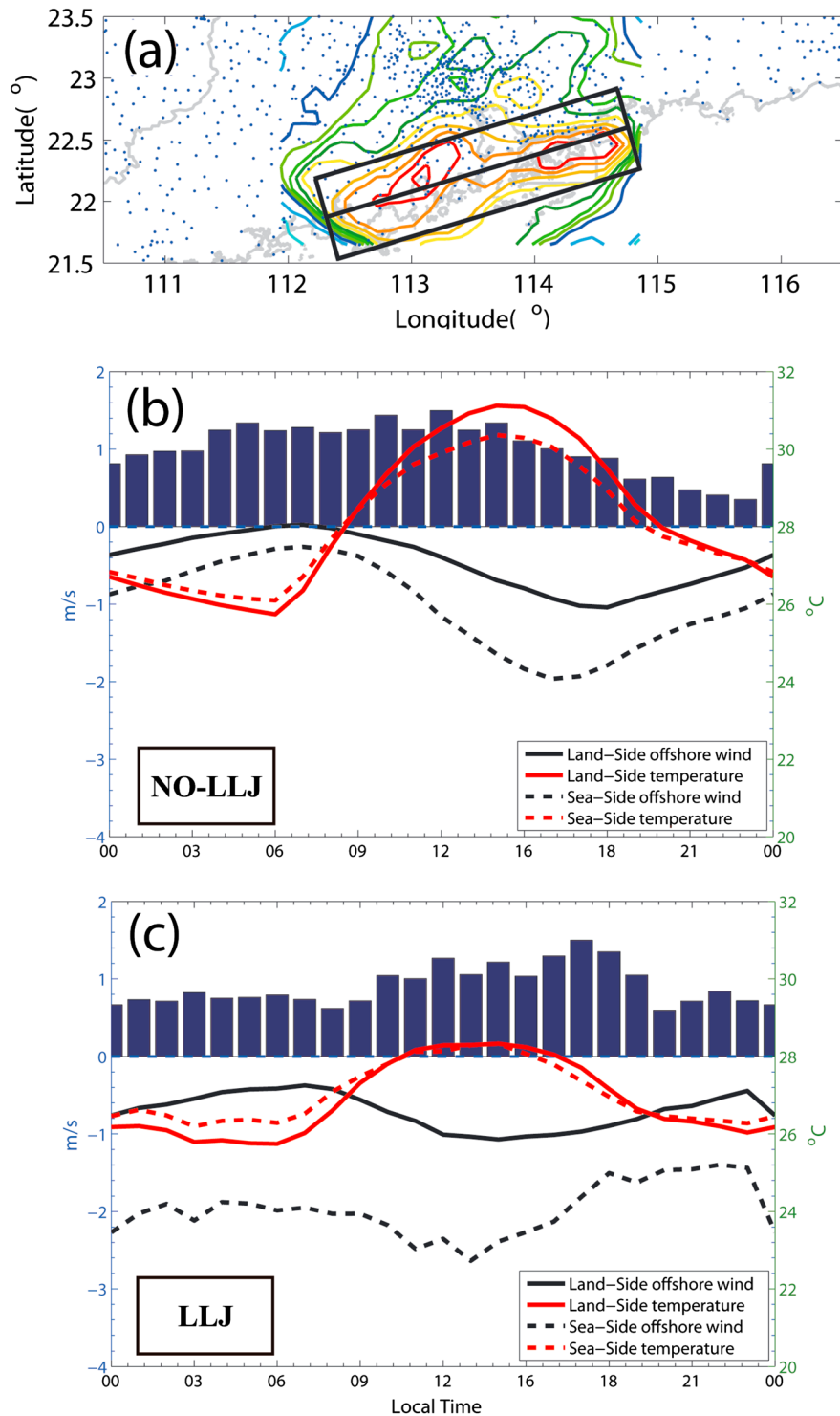


**Figure 11.** Spatial distribution of (a) automatic weather stations, with color contours being convection occurrence frequency on LLJ days and the black rectangles indicating two subregions along the coast. Diurnal change of surface temperature (red lines), offshore wind (black lines), and precipitation (blue bars) in (b) no-LLJ and (c) LLJ days.

The coastal precipitation on LLJ days seems to have a very different diurnal pattern. Rainfall occurs mostly during the afternoon, peaking at 17:00 LST; this pattern is similar to the diurnal cycle of convective features in the entire warm season. The dominant triggering and maintenance mechanisms of coastal convection during LLJ and no-LLJ days are therefore quite different. The exact reasons for such differences

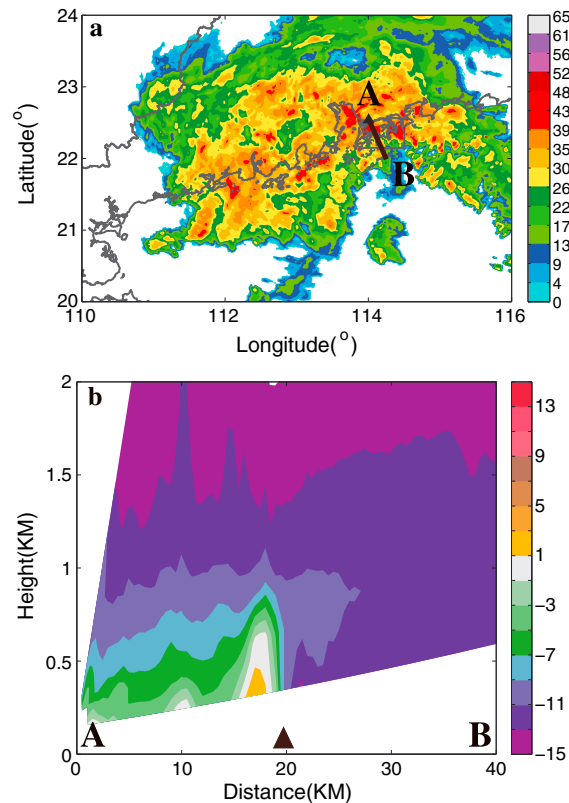


**Figure 12.** (a) Composite (column maximum) reflectivity mosaic at 22:10 UTC 23 May 2009. (b) Vertical cross section along black line AB in Figure 12a of the 2 day average radial velocity.

will require further study, and more samples for the LLJ days will also help make the results statistically more robust.

To help us to further understand the processes, we picked several cases for a more detailed study. One of them is a 2 day precipitation episode from May 2009 with the presence of LLJ (Figure 12a). This case was chosen because it was a representative one, producing strong precipitation along the coastline but without inland precipitation. In this period, convection moved from the sea and strengthened after it reached the coastline. New convective cells were initiated along the coastline. Two quasi-linear convective systems were present during this episode. Figure 12b is the vertical cross section of the 2 day average radial velocity obtained from Shenzhen Radar (denoted as "A" in Figure 12a). The cross-section line AB is shown in Figure 12a with the composite reflectivity mosaic, and the coastline is about 20 km from the radar (black triangle in Figure 12b). During this precipitation episode, environmental winds at the low levels were onshore, as indicated by the negative radial velocity in Figure 12b at the lower levels. After the near-surface (below 500 m) flow reached the coastline, the wind speed decreased dramatically (changing from  $-15 \text{ m s}^{-1}$  to

about  $0 \text{ m s}^{-1}$ ), apparently due to increased surface drag; as a result, strong velocity convergence is found across the coastline. The small region of positive (offshore, about  $1 \text{ m s}^{-1}$ ) radial velocity on the landside of coastline must have been induced by the convection triggered by the convergence. Although this convergence may have been enhanced by the coastal convection, the change in the roughness should be the initial cause for the convergence, and it anchors the main convergence zone along the coastline.

## 6. Summary and Conclusions

Convective precipitation is the main cause of meteorological disasters in south China in the warm season, defined as the months of May through September in this study. The Pearl River Delta (PRD) region, one of the most important economic and population centers in China, is also a climatological rainfall center in south China. In the region, convective rainfall accounts for more than 45% of the total rainfall during warm season. In this paper, the spatial and temporal characteristics, including the horizontal distributions, vertical depths, and diurnal cycles of convection in the region as well as their monthly variations throughout the warm season and their relationship with general changes in large scale conditions are studied using the data from operational weather radars of 3 years and data from automatic surface stations. Gridded reanalysis data from JMA are used to examine the mean meteorological conditions, including flow patterns and temperature and moisture distributions.

Convective features are first identified based on the radar reflectivity data. Precipitation is also estimated from the radar data. Over the entire 5 month period, two main centers of high convection frequency are found in the PRD region. One is along the southern coastline, and the other is roughly on the windward slope of mountains in the northeastern part of the region. Excluding days with strong synoptic scaling forcing, namely, days with strong fronts or TC, does not change the precipitation distribution much. Forcing associated with the topography and coastline therefore clearly plays dominant roles. Among all convective

features, larger and deeper features show much more clear concentration in the two high-frequency regions, while smaller and shallower convective features show no obvious spatial preference in the region.

In the 5 months of the warm season, convection shows clear but different diurnal cycles. All months have their primary peak in the early afternoon between 14:00 and 15:00 LST, with August and July having the most prominent, single peak throughout the 24 h. May and June have a secondary peak in the early morning, and September has a secondary peak in early evening. Land-sea breeze activities are suggested to be the cause of the early morning peak in May and June, while the cause of the early evening peak is not clear (not the focus of this study). The depth of strong convection increases as the season progresses from May through August but is decreased in September, and such seasonal changes are linked to the changes in synoptic weather patterns and changes in solar heating. There are also clear changes in the spatial distribution of convection from month to month. In May, the maximum along the coastline is less obvious, while August and September have no prominent inland frequency maximum. The change in the distribution is linked to the changes in the direction of low-level prevailing winds.

A mean wind profile throughout the warm season is derived from the radar radial velocity data using the VAD technique. A single wind speed maximum is found in the profile at about 2.3 km altitude, representing a low-level jet (LLJ). No boundary layer LLJ at a lower altitude is found, as is the case with some other parts of the mainland China and the Taiwan region.

Excluding the days influenced by strong frontal systems or TC, on LLJ days, the convection frequency maximum along the coast is prominent but not inland. In contrast, frequency maximum is mainly found at the foot of the northeastern mountains on no-LLJ days on average. On LLJ days, the mean updraft motion is stronger at the coast in the reanalysis data. Automatic surface station data indicate stronger low-level convergence at the coast, apparently induced by differential surface friction across the land and ocean boundary. On no-LLJ days, the coastal convergence is weaker on average, allowing onshore flows to cross the coastal region without triggering convection and reach the mountain slope to the north where orographic lifting produces the precipitation maximum in that part of the region.

While some of the findings of this study are similar to those of a few earlier studies based on satellite data, the much high spatial and temporal resolutions of the radar data over the 3 years over the study period, in combination with regional reanalysis and automatic surface station data and the VAD-derived wind profiles, allowed us to examine in much more detail the horizontal and vertical structures of convection, spatial distributions of precipitation in relation to coastline and orography, and diurnal variations down to hourly time scales. These characteristics are linked to seasonally varying flow and thermodynamic conditions and to strong low-level prevailing winds in the form of low-level jets. Differential surface friction across the coastline is believed to be the key cause of coastal precipitation maximum, although a firm conclusion will require more detailed investigations.

#### Acknowledgments

This work was primarily supported by the National Fundamental Research 973 Program of China (2013CB430100) and Social Common wealth Research Program (GYHY201006007 and GYHY200906004), and the National Natural Science Foundation of China (grants 41275031 and 41322032). We would also like to acknowledge the China Meteorological Administration for collecting and archiving the radar data used in this study. Data used in this work are from the National Fundamental Research 973 Program of China (2013CB430101).

#### References

- Browning, K. A., and R. Wexler (1968), The determination of kinematic properties of a wind field using doppler radar, *J. Appl. Meteorol.*, 7(1), 105–113.
- Chelton, D. B., M. H. Freilich, and S. K. Esbensen (2000), Satellite observations of the wind Jets off the Pacific Coast of Central America. Part I: Case studies and statistical characteristics, *Mon. Weather Rev.*, 128(7), 1993–2018.
- Chen, G., Y. Zheng, and T. Xiao (2011), Distribution and spatiotemporal variations of deep convective clouds over China during the warm season [in Chinese], *Meteorolog. Mon.*, 37(1), 75–84.
- Chen, G. T.-J. (1983), Observational aspects of the Mei-Yu phenomenon in subtropical China, *J. Meteor. Soc. Jpn.*, 61, 306–312.
- Chen, G. T.-J., and C.-C. Yu (1988), Study of low-level jet and extremely heavy rainfall over Northern Taiwan in the Mei-Yu Season, *Mon. Weather Rev.*, 116, 884–891.
- Chen, G. T.-J., C.-C. Wang, and D. T.-W. Lin (2005), Characteristics of low-level jets over Northern Taiwan in Mei-Yu Season and their relationship to heavy rain events, *Mon. Weather Rev.*, 133, 20–43.
- Chen, T.-J. G., and C.-P. Chang (1980), The structure and vorticity budget of an early summer monsoon trough (Mei-Yu) over Southeastern China and Japan, *Mon. Weather Rev.*, 108(7), 942–953.
- Chen, Y.-L., and S.-F. Tseng (2000), Comments on “The intensification of the low-level jet during the development of mesoscale convective systems on a Mei-Yu Front”, *Mon. Weather Rev.*, 128(2), 495–506.
- Chen, Y.-L., X. A. Chen, and Y.-X. Zhang (1994), A Diagnostic study of the low-level jet during TAMEX IOP 5, *Mon. Weather Rev.*, 122(10), 2257–2284.
- Cho, H.-R., and G. T. J. Chen (1995), Mei-Yu Frontogenesis, *J. Atmos. Sci.*, 52(11), 2109–2120.
- Crum, T. D., R. L. Alberty, and D. W. Burgess (1993), Recording, archiving, and using WSR-88D Data, *Bull. Am. Meteorol. Soc.*, 74(4), 645–653.
- Ding, Y. (2010), *Monsoons Over China*, pp. 420, Springer.
- Donaldson, R. J. (1961), Radar reflectivity profiles in thunderstorms, *J. Meteorol.*, 18(3), 292–305.

- Douglas, M. W., A. Valdez-Manzanilla, and R. Garcia Cueto (1998), Diurnal variation and horizontal extent of the low-level jet over the Northern Gulf of California, *Mon. Weather Rev.*, *126*(7), 2017–2025.
- Du, Y., Q. Zhang, Y. Yue, and Y. Yang (2012), Characteristics of low-level jets in Shanghai during the 2008–2009 warm seasons as inferred from wind profiler radar data, *J. Meteorol. Soc. Jpn.*, *90*, 891–903.
- Du, Y., Q. Zhang, Y.-L. Chen, Y. Zhao, and X. Wang (2014), Numerical simulations of spatial distributions and diurnal variations of low-level jets in China during early summer, *J. Clim.*, *27*, 5747–5767.
- Fulton, R. A., J. P. Breidenbach, D.-J. Seo, D. A. Miller, and T. O'Bannon (1998), The WSR-88D Rainfall Algorithm, *Weather Forecasting*, *13*(2), 377–395.
- Georgelin, M., E. Richard, and M. Petidier (1996), The impact of diurnal cycle on a low-froude number flow observed during the pyrex experiment, *Mon. Weather Rev.*, *124*(6), 1119–1131.
- Holleman, I. (2005), Quality control and verification of weather radar wind profiles, *J. Atmos. Oceanic Tech.*, *22*, 1541–1550.
- Igau, R. C., and J. W. Nielsen-Gammon (1998), Low-level jet development during a numerically simulated return flow event, *Mon. Weather Rev.*, *126*(11), 2972–2990.
- Jou, B. J.-D., and S.-M. Deng (1992), Structure of a low-level jet and its role in triggering and organizing moist convection over Taiwan: A TAMEX case study, *Terr. Atmos. Oceanic Sci.*, *3*, 39–58.
- Jou, B. J.-D., and S.-M. Deng (1998), The organization of Convection in a Mei-Yu frontal rainband, *Terr. Atmos. Oceanic Sci.*, *4*, 533–572.
- Kuo, Y.-H., L. Cheng, and J.-W. Bao (1988), Numerical Simulation of the 1981 Sichuan Flood. Part I: Evolution of a Mesoscale Southwest Vortex, *Mon. Weather Rev.*, *116*(12), 2481–2504.
- Li, J., and Y.-L. Chen (1998), Barrier jets during TAMEX, *Mon. Weather Rev.*, *126*(4), 959–971.
- Li, J., R. Yu, and T. Zhou (2008), Seasonal variation of the diurnal cycle of rainfall in Southern Contiguous China, *J. Clim.*, *21*(22), 6036–6043.
- Liu, P., and Y. Fu (2010), Climatic characteristics of summer convective and stratiform precipitation in southern China based on measurement by TRMM precipitation radar [in Chinese], *Chin. J. Atmos. Sci.*, *34*(4), 802–814.
- Luo, Y., H. Wang, R. Zhang, W. Qian, and Z. Luo (2012), Comparison of rainfall characteristics and convective properties of monsoon precipitation systems over south china and the yangtze and huai river basin, *J. Clim.*, *26*(1), 110–132.
- Marshall, J. S., and W. M. K. Palmer (1948), The distribution of raindrops with size, *J. Meteorol.*, *5*(4), 165–166.
- Mohr, C. G., and R. L. Vaughan (1979), An economical procedure for cartesian interpolation and display of reflectivity factor data in three-dimensional space, *J. Appl. Meteorol.*, *18*(5), 661–670.
- Nelson, S., F. H. Carr, and L. J. Ruthi (1995), Intercomparison of horizontal velocities observed by modern wind-finding systems, in *Preprints, Ninth Symp. Meteor. Observations Instrumentation*, pp. 5, Am. Meteorol. Soc., Charlotte, N. C.
- Romatschke, U., and R. A. Houze (2011), Characteristics of precipitating convective systems in the south asian monsoon, *J. Hydrometeorol.*, *12*(1), 3–26.
- Romatschke, U., S. Medina, and R. A. Houze (2010), Regional, seasonal, and diurnal variations of extreme convection in the south asian region, *J. Clim.*, *23*(2), 419–439.
- Saito, K., et al. (2006), The operational jma nonhydrostatic mesoscale model, *Mon. Weather Rev.*, *134*(4), 1266–1298.
- Skamarock, W. C., R. Rotunno, and J. B. Klemp (1999), Models of coastally trapped disturbances, *J. Atmos. Sci.*, *56*(19), 3349–3365.
- Smith, R. B., and V. Grubišić (1993), Aerial observations of Hawaii's wake, *J. Atmos. Sci.*, *50*(22), 3728–3750.
- Steiner, M., R. A. Houze Jr., and S. E. Yuter (1995), Climatological characterization of three-dimensional storm structure from operational radar and rain gauge data, *J. Appl. Meteorol.*, *34*, 1978–2007.
- Sun, J. (2012), Evolution and structure of a convection line over coastal region of South China in June 2008 [in Chinese], *Torrential Rain And Disasters*, *31*(3), 201–209.
- Szoke, E. J., and E. J. Zipser (1986), A Radar study of convective cells in mesoscale systems in gate. Part II: Life cycles of convective cells, *J. Atmos. Sci.*, *43*(2), 199–218.
- Tai-Jen Chen, G., and C.-C. Yu (1988), Study of low-level jet and extremely heavy rainfall over Northern Taiwan in the Mei-Yu Season, *Mon. Weather Rev.*, *116*(4), 884–891.
- Ulbrich, C. W., and L. G. Lee (1999), Rainfall Measurement Error by WSR-88D Radars due to Variations in Z-R Law Parameters and the Radar Constant, *J. Atmos. Oceanic Tech.*, *16*(8), 1017–1024.
- Xu, W. (2013), Precipitation and convective characteristics of summer deep convection over East Asia observed by TRMM, *Mon. Weather Rev.*, *141*(5), 1577–1592.
- Xu, W., and E. J. Zipser (2011), Diurnal variations of precipitation, deep convection, and lightning over and east of the eastern tibetan plateau, *J. Clim.*, *24*(2), 448–465.
- Xu, W., and E. J. Zipser (2012), Properties of deep convection in tropical continental, monsoon, and oceanic rainfall regimes, *Geophys. Res. Lett.*, *39*, L07802, doi:10.1029/2012GL051242.
- Xu, W., E. J. Zipser, and C. Liu (2009), Rainfall characteristics and convective properties of Mei-Yu precipitation systems over South China, Taiwan, and the South China Sea. Part I: TRMM Observations, *Mon. Weather Rev.*, *137*(12), 4261–4275.
- Xu, W., E. J. Zipser, Y.-L. Chen, C. Liu, Y.-C. Liou, W.-C. Lee, and B. J.-D. Jou (2012), An orography-associated extreme rainfall event during TiMREX: Initiation, storm evolution, and maintenance, *Mon. Weather Rev.*, *140*, 2555–2574.
- Xu, X., K. Howard, and J. Zhang (2008), An automated radar technique for the identification of tropical precipitation, *J. Hydrometeorol.*, *9*(5), 885–902.
- Yu, C.-K., and B. J.-D. Jou (2005), Radar observations of the diurnally forced offshore convective lines along the southeastern coast of Taiwan, *Mon. Weather Rev.*, *133*(6), 1613–1636.
- Yu, R., and J. Li (2012), Hourly rainfall changes in response to surface air temperature over Eastern Contiguous China, *J. Climate*, *25*(19), 6851–6861.
- Yuan, W., R. Yu, H. Chen, J. Li, and M. Zhang (2010), Subseasonal characteristics of diurnal variation in summer monsoon rainfall over Central Eastern China, *J. Clim.*, *23*(24), 6684–6695.
- Zhang, C.-Z., H. Uyeda, H. Yamada, B. Geng, and Y. Ni (2006), Characteristics of mesoscale convective systems over the east part of continental China during the Meiyu from 2001 to 2003, *J. Meteorol. Soc. Jpn.*, *84*, 763–782.
- Zhang, C.-Z., Q.-L. Wan, Z.-L. Yao, W.-Y. Ding, Z.-T. Chen, and Y.-Y. Huang (2011), Characteristic analysis of structure and lightning for convective system produced heavy precipitation in warm sector of south China [in Chinese], *Plateau Meteorol.*, *30*(4), 1034–1045.
- Zhang, J., and Y. Qi (2010), A Real-Time algorithm for the correction of brightband effects in radar-derived QPE, *J. Hydrometeorol.*, *11*(5), 1157–1171.
- Zhang, J., and S. Wang (2006), An automated 2D multipass Doppler radar velocity dealiasing scheme, *J. Atmos. Oceanic Tech.*, *23*, 1239–1248.

- Zhang, J., S. Wang, and B. Clarke (2004), WSR-88D reflectivity quality control using horizontal and vertical reflectivity structure, paper presented at Preprints, 11th conference Aviation, Range, and Aerospace Meteor., Amer. Meteor. Soc., Hyannis, Mass.
- Zheng, Y., and J. Chen (2011), A climatology of deep convection over south China and adjacent seas during summer [in Chinese], *J. Trop. Meteorol.*, *27*(4), 495–508.
- Zhou, T., R. Yu, H. Chen, A. Dai, and Y. Pan (2008), Summer precipitation frequency, intensity, and diurnal cycle over China: A Comparison of Satellite Data with Rain Gauge Observations, *J. Clim.*, *21*(16), 3997–4010.
- Zhu, X., Y. Zheng, L. Guo, and Z. Tao (2010), Distribution and spatiotemporal Variations of Deep Convection over Guangdong and Adjacent Areas during Heavy Rainfall Period of 2008 [in Chinese], *Acta Sci. Nat. Univ. Pekin.*, *46*(5), 784–792.
- Zipser, E. J., and K. R. Lutz (1994), The vertical profile of radar reflectivity of convective cells: a strong indicator of storm intensity and lightning probability?, *Mon. Weather Rev.*, *122*(8), 1751–1759.